Front. Earth Sci. 2018, 12(4): 808–817
https://doi.org/10.1007/s11707-016-0653-0

RESEARCH ARTICLE

Interpretation of gravity data for fault distribution near the Mongolia–Hinggan metallogenic belt in the eastern China-Mongolia frontier area

Jun WANG (✉)[1,2], Xiaohong MENG (✉)[1,2], Zhaoxi CHEN[1,2], Fang LI[3]

1 Key Laboratory of Geo-detection (China University of Geosciences, Beijing), Ministry of Education, Beijing 100083, China
2 School of Geophysics and Information Technology, China University of Geosciences, Beijing 100083, China
3 China Aero Geophysical Survey and Remote Sensing Center for Land and Resources, Beijing 100083, China

Abstract The Central Asian Orogenic Belt (CAOB) is a giant suture zone produced by the reduction of the Paleo-Asian Ocean between the Siberian, North China, and Tarim cratons. The CAOB formed in three main stages, including continental accretion, late collision, and intra-continental orogeny. Strong crust-mantle interaction also occurred during these stages. The eastern China-Mongolia frontier area is an important part of the CAOB. Since the Caledonian period, this region has frequently experienced polycyclic tectonic reformation and intense magmatic activities. All of these geological activities lay the foundation for abundant metal resources. In the past, several large metal ore deposits have been founded there. However, the deep structure of different tectonic units and the fault distribution in the eastern China-Mongolia border frontier area are still not clear owing to the complex geological environment. Existing works in that region are insufficient for an in-depth understanding of the metallogenic deposits. The work discussed in this paper was carried out in the eastern China-Mongolia frontier area with measured gravity data along a profile and gravity data extracted from the WGM2012 earth's gravity model for detailed fault distribution. In this study, empirical mode decomposition (EMD) and tilt angle analysis (TDR) were utilized for processing the gridded gravity data. The measured gravity data were inverted with a 2D inversion algorithm for density distribution along the survey line. The inversion result was used to verify the existence of known faults and describe their deeper extensions. Meanwhile, new faults were also identified along the survey line and then marked on the gridded data to get their horizontal distribution. These results provide significant information for the in-depth understanding of the tectonic units in the study area.

Keywords the CAOB, China-Mongolia frontier area, gravity data, processing and inversion, fault distribution

1 Introduction

Central Asia is a gigantic complex composed of various terranes including Precambrian continental blocks, ancient island arcs, ophiolites, and passive continental margins. These terranes were amalgamated from the late Precambrian/early Paleozoic to the late Mesozoic (Jahn et al., 2004). During this period, various geological activities formed the world's largest Phanerozoic orogenic belt – the Central Asian Orogenic Belt (CAOB). The CAOB is a classic example of an accretionary orogeny, which was produced by the reduction of the Paleo-Asian Ocean between the Siberian, North China, and the Tarim cratons. Its formation represents a complex evolution of orogenic belts. During its evolution the CAOB experienced three main stages, including continental accretion, late collision, and intracontinental orogeny. Strong crust-mantle interaction also occurred. The CAOB records the accretion history of the arcs and microcontinents over a time span of about 400 Ma. The eastern China-Mongolia frontier area is an important part of the CAOB, consisting of complex tectonic magmatic belts and fault zones. Since the Caledonian period, this region has experienced polycyclic tectonic reformation and frequent, intense magmatic activities. Throughout the whole evolutionary process, convergence of the Paleo-Asian Ocean along with the deep mantle plume activity played a leading role (Mossakovsky et al., 1993; Jahn et al., 2004; Metcalfe, 2006; Didenko

Received November 25, 2016; accepted June 14, 2018

E-mails: wangjun5505@163.com (Jun WANG); mxh@cugb.edu.cn (Xiaohong MENG)

et al., 2010; Xiao et al., 2010; Yarmolyuk et al., 2014). All of these geological activities laid the foundation for abundant metal resources.

Over the past years, many large non-ferrous metal ore deposits have been found near the eastern China-Mongolia frontier area based on geological and geophysical surveys. Research indicates this area, along with the adjacent regions, may become a hot spots for prospecting in this century (Perello et al., 2001; Nie et al., 2004). However, the deep structural characteristics of the different tectonic units and fault distribution in this area are still not clear owing to the complex geological environment. Existing works on this region are insufficient for an in-depth understanding of the metallogenic and prospecting possibilities.

The work discussed in this paper has been carried out near the Mongolia–Hinggan metallogenic belt in the eastern China-Mongolia frontier area with gravity data acquired from different sources. As we all know, gravity data have played an important role in various geologic and geophysical investigations. Rational interpretation of gravity data often highlights individual geological bodies in the context of complex regional tectonic settings (Nabighian et al., 2005; Uieda and Barbosa, 2012; Guo et al., 2014; Wang et al., 2014, 2015a;Yan et al., 2014; Liu et al., 2015). Moreover, gravity data have been used to identify fault distribution in existing researches.

In this study, field gravity data were measured along the Mongolia–Hinggan metallogenic belt. Gridded gravity data in the near area of this belt were extracted from the WGM2012 earth's gravity model (Balmino et al., 2012). Both of the gravity datasets were separated with the EMD technique to get residual and regional gravity anomalies, which were then utilized for identification of lineaments in the upper and deeper crust, respectively. The gridded gravity data were analyzed with the TDR method for linear feature enhancement. The measured gravity data were inverted with a 2D physical parameter inversion algorithm for density distribution along the survey line. The inversion result was used to verify the existing faults and to describe their deeper extensions. Moreover, the density distribution was also used for identification of new faults along with linear features of the gridded gravity data. The results of this study provide significant information for a deeper understanding of the tectonic units in the eastern China-Mongolia frontier area, which helps the understanding of the metallogenic and prospecting possibilities.

2 Research area and data sources

The research area is located in the eastern China-Mongolia

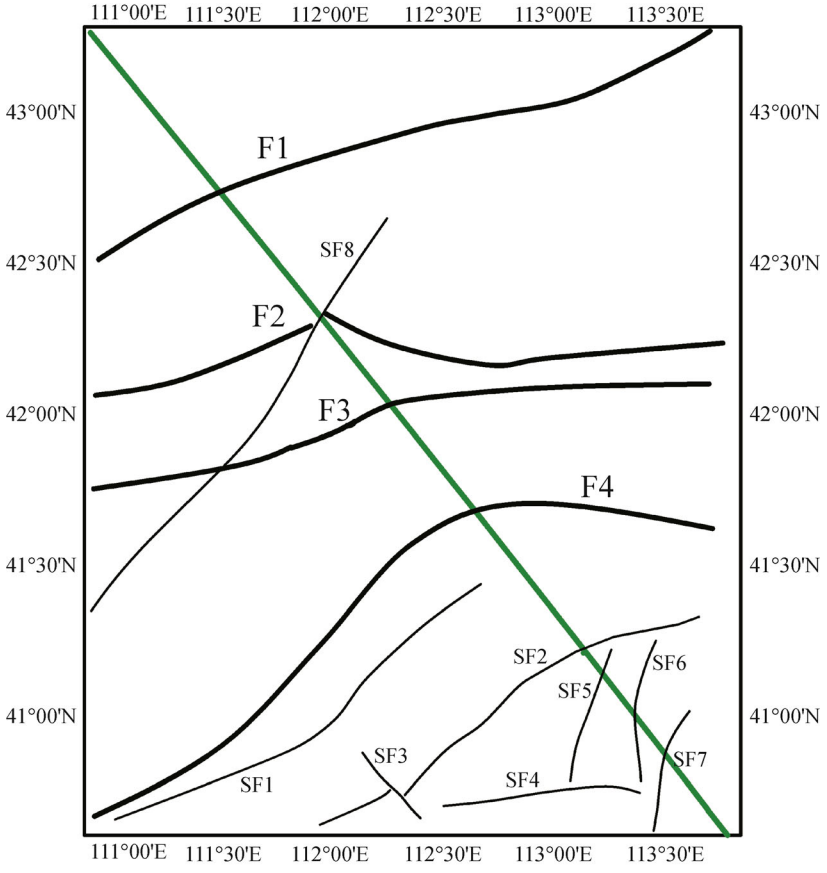

Fig. 1 Map showing location of the research area.

frontier area, shown in Fig. 1 with the black rectangle. The research area is within the intersection of the Hinggan–Mongolian orogenic belt and the northern margin of the North China craton. Outcrops of Archaeozoic–Cenozoic strata are widespread. The majority of mineral resources in this area are distributed around the Mongolia-Hinggan Orogenic belt, along which gravity measurements were conducted, shown in Fig. 1 with the solid green line. The survey line is perpendicular to the main structural trend and cuts across some significant faults. Brief descriptions of the existing faults are given in Table 1.

Field gravity measurements were taken from 2010 to 2012. The survey line was about 400 km long with 4800 gravity data points and about 650 check points. The mean square error of the gravity measurement is $\pm 0.036 \times 10^{-5}$ m/s^2. Figure 2(a) shows the corrected Bouguer gravity data along the survey line. Amplitude of the gravity data ranges from -120×10^{-5} m/s^2 to -160×10^{-5} m/s^2 in most areas along the line except three low regions where the lowest gravity value is about -190×10^{-5} m/s^2.

Gridded Bouguer gravity data were extracted from the WGM2012 earth's gravity model. Referencing Balmino et al. (2012), the WGM2012 gravity model is derived from the available earth global gravity models EGM2008 and DTU10. Moreover, it includes 1'×1' resolution terrain corrections derived from the ETOPO1 model that consider the contribution of most surface masses (Amante and Eakins, 2009). The gravity data have been computed by means of a spherical harmonic approach using theoretical developments carried out to achieve accurate computations at global scale. Figure 3(a) shows the Bouguer gravity data in the research area. It can be see that the values of the gravity data are relatively large in the northern part and the southeastern corner. The minimal values are located in the middle of the area.

3 Gravity data processing

The flow chart of the research is displayed in Fig. 4. The utilized techniques include gravity anomaly separation based on EMD, TDR analysis for linear feature enhancement, and 2D physical inversion for density distribution. In the following sections, a brief description of each is given.

3.1 Gravity anomaly separation based on EMD

The EMD method was first proposed by Huang et al. (1998) to analyze nonlinear and non-stationary signals. The input signal is decomposed into individual components with different frequencies, called intrinsic mode functions (IMFs) (Ali-Rahim, 2016). The original signal can be reconstructed by summing all of the IMFs with no loss of information. The EMD method does not depend on the primary basis function as is required for the Fourier and wavelet analysis methods. It is an adaptive technique and has been widely used in signal processing (Li and Ji, 2009), texture analysis (Nunes et al., 2005), and random noise attenuation (Chen and Ma, 2014).

Huang et al. (1998) defined that any IMF should satisfy two specifications: 1) the difference between the number of extreme points (maxima and minima points) and the number of zero crossing points must be less than one; 2) the mean of the envelope defined by the local maxima point and local minima point should be zero for any part of the signal. We applied this method for the separation of gravity data.

The detailed steps are:

1) Input the gravity data as $x(n)$, identify all the local extrema points, including the local maxima points and minima points.

2) Interpolate between these extrema points to produce

Table 1 Descriptions of the existing major faults

Number	Name	Description
F1	Sauron–Ulanhot fault	✔**Scale**: Deep fault; ✔ **Strike (northeast)**: Sauron aobao of Urad Middle Banner–Chagan hada of Damao Banner–Sonid Right Banner–Silas MuLun River–Jarud Banner–Ulanhot; ✔ **Dip**: East-west in the west and middle part, gradually changes to the north-east
F2	Gaojia kiln–White City fault	✔**Scale**: Deep fault; ✔**Strike (west to east)**: The north mountain–the Cut well–Langshan–Bayan Obo–Huade–Ongniud Banner–Kailu–the White City; ✔**Dip**: East-west
F3	Wuyuan–Chifeng fault	✔**Scale**: Deep fault; ✔**Strike (west to east)**: Wuyuan–Taipusi Banner–Weichang–Chifeng; ✔**Dip**: East-west
F4	Linhe–Harqin Banner fault	✔**Scale**: Deep fault; ✔**Strike (northeast then turning east-west)**: Linhe–Urad Front Banner–Wuchuan–Chahar Right Middle Banner–Jining; ✔**Dip**: East-west

Note: Terminology used in above table to describe faults is incorrect. Strike is the direction of the line formed by the intersection of the fault with the earth's surface. Dip is always perpendicular to strike and refers to the angle the fault surface makes with the earth's surface. No information is given in the table as to the direction of the fault movements.

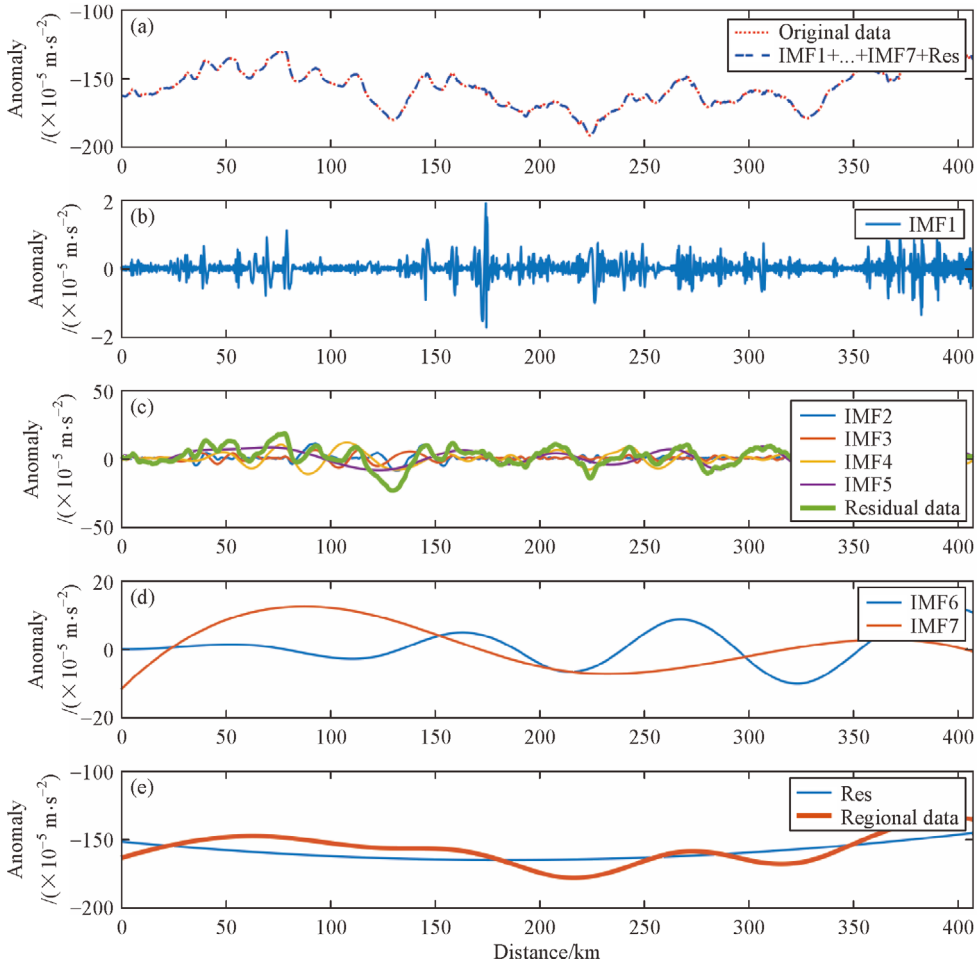

Fig. 2 (a) Bouguer gravity along the settled profile; (b)−(e) various intrinsic mode functions of the empirical mode decomposition of the measured gravity anomaly. The 'Res' can be expressed as Res = Original data – (IMF1 + IMF2 +…+ IMF7).

upper and lower envelope limits, i.e., Max(n) and Min(n).

3) Calculate the average signal, Mean(n) = mean (Max(n), Min(n)).

4) Calculate $d(n) = x(n) - \text{Mean}(n)$, and check if $d(n)$ meets the above specifications for IMF. If the condition is satisfied, $d(n)$ is the first IMF. If the condition is not satisfied, screening of the above procedures is repeated until the result satisfies the definition of IMF.

5) Use $x(n) - IMF_1$ as the new input data, and repeat the above process to obtain various IMFs.

The final IMF which had very few extreme points was treated as the regional gravity data and the sum of the others was considered as the residual gravity data. Figure 2 shows some IMFs of the measured gravity data. Figure 2 (b) is the first IMF which has very low amplitude and high frequency and was treated as noise. The sum of IMF2–IMF5 was the separated residual gravity data, while others were the regional data. The residual data would be used for inversion to get the density distribution in the upper crust along the survey line.

For the gridded gravity data, a similar procedure was performed by BEMD method (bidimensional empirical mode decomposition). Figures 3(b) and 3(c) are the separated residual and regional gravity data, respectively. Results suggest that the regional Bouguer gravity data decrease rapidly from northeast to southwest, causing isostatic adjustment and showing a decrease in crustal density. The residual Bouguer gravity data in the northern part of the area is relatively large. The residual and regional data would be utilized for linear features detection in the shallow and deeper crust.

3.2 Linear features enhancement with TDR

The TDR was introduced by Miller and Singh (1994) and Verduzco et al. (2004) as

$$\text{TDR} = \tan^{-1}\left(\frac{\partial g/\partial z}{\sqrt{(\partial g/\partial x)^2 + (\partial g/\partial y)^2}}\right), \quad (1)$$

where g denotes the inputted gravity data, $\partial g/\partial z$ is the

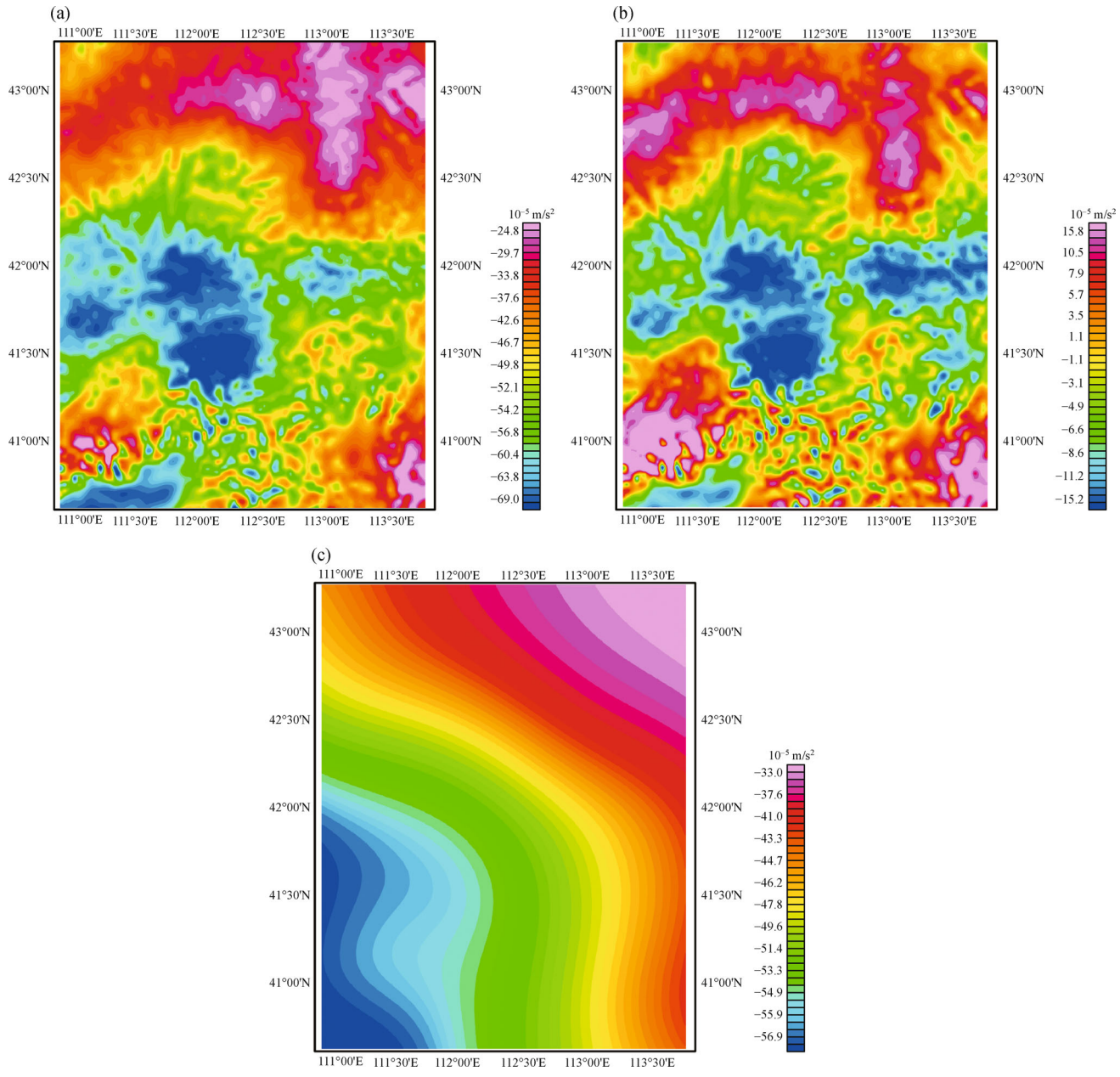

Fig. 3 (a) Bouguer gravity data extracted from the WGM2012 earth's gravity model; (b) The separated residual gravity data based EMD; (c) The separated regional gravity data based EMD.

vertical derivative, and $\sqrt{(\partial g/\partial x)^2 + (\partial g/\partial y)^2}$ is the horizontal derivative (Ghosh, 2016).

The value of Eq. (1) varies between $+\pi/2$ and $-\pi/2$ radians. TDR is 0 radians at the measuring point ($x = x0$) above the edges of the contact. This property identifies the horizontal location of the geological sources. The TDR analysis for fault location has been carried out by many researchers (Blakely and Simpson, 1986; Miller and Singh, 1994; Fedi and Florio, 2001; Williams et al., 2005; Phillips et al., 2007; Oruç, 2011; Ghosh, 2016).

The TDR analysis was performed in this study for linear features enhancement. Figures 5(a) and 5(b) are the TDR results of the residual and regional gravity data, respectively. They show that the trends of most of the major faults (F1–F4) are in good agreement with the linear features contained in the regional gravity data. This verifies that F1–F4 are the major deep faults corresponding to the units' boundaries. For the smaller faults, SF1, SF2, and SF8 are obvious in the TDR of regional gravity data. SF3–SF7 can be found in the features of the TDR of residual gravity data. The TDR result will be utilized for fault interpretation in the following section.

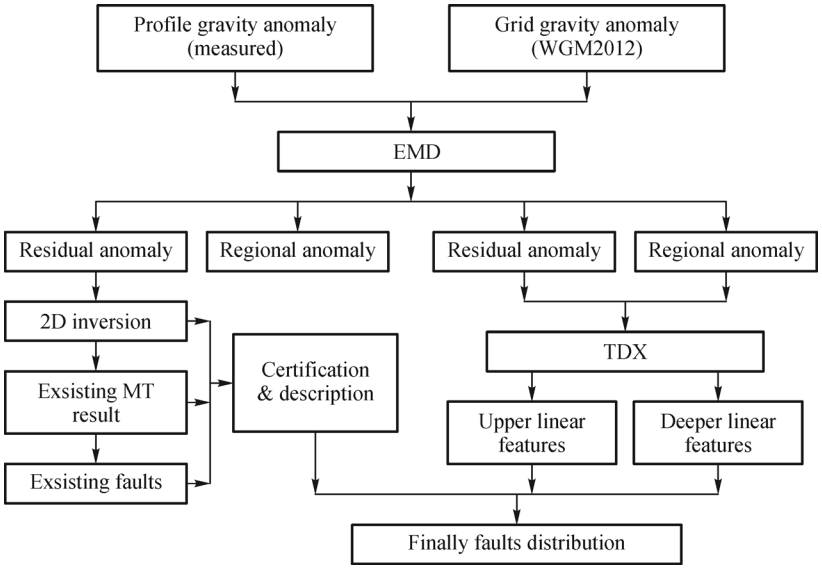

Fig. 4 Flow chart of the researches conducted in this study.

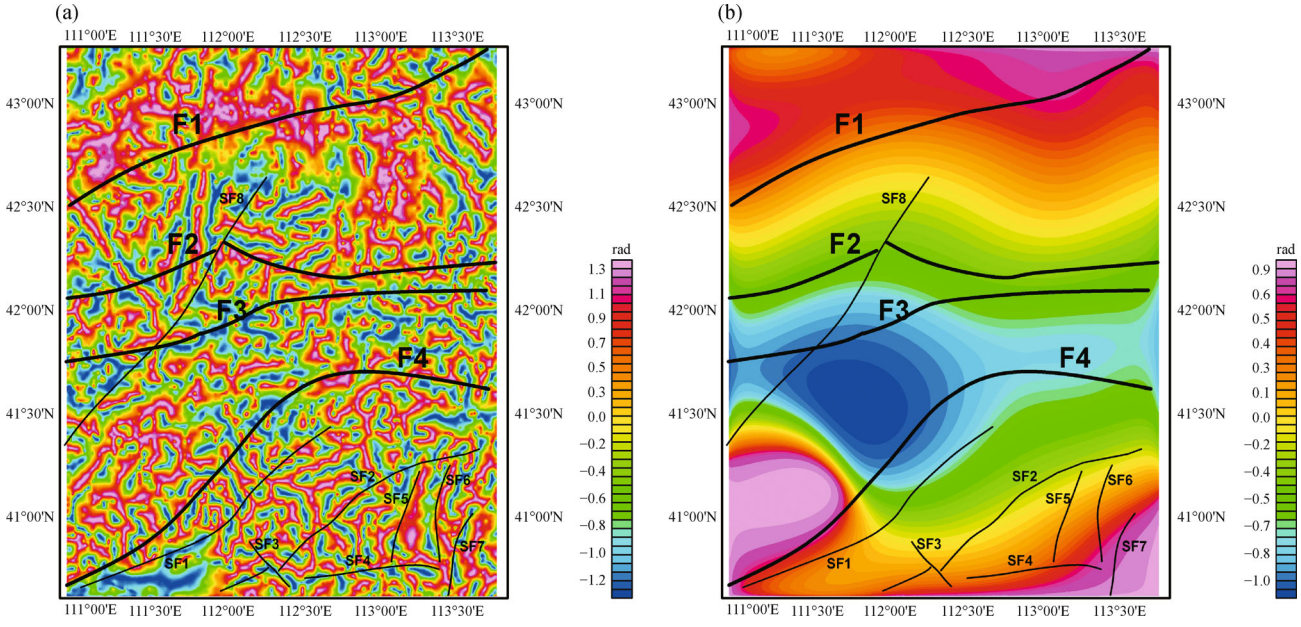

Fig. 5 (a) TDR analysis of the residual gravity data; (b) TDR analysis of the regional gravity data. In these two figures, the black lines denote existing faults.

3.3 2D density inversion

In this study, the measured gravity data was inverted with the algorithm proposed by Li and Oldenburg (1998). The subsurface is considered as a gridded system with constant physical properties (density) in each cell. The goal of the inversion is to calculate the property of each cell. The inversion problem can be expressed as

$$Gm = d, \tag{2}$$

where d is the observed data, G is the kernel matrix, and m is the model parameter to be determined. For the inversion of gravity data, the number of model parameters is much greater than the number of data points. So, the problem expressed in Eq. (2) is an underdetermined problem which is ill-posed. A model objective function as Eq. (3) is utilized to limit the solution space,

$$\phi_m = \alpha_s \int_v w_s [w_r(z)(m - m_{ref})]^2 \mathrm{d}v + \alpha_x \int_v w_x \left[\frac{\partial \left(w_r(z)(m - m_{ref}) \right)}{\partial x} \right]^2 \mathrm{d}v$$

$$+\alpha_z \int_v w_z \left[\frac{\partial\left(w_r(z)(m-m_{ref})\right)}{\partial z}\right]^2 \mathrm{d}v, \qquad (3)$$

where m_{ref} is the reference model, $w_r(z)$ is the depth weighting function, w_s, w_x, and w_z are the weighted functions, and α_s, α_x, and α_z are the coefficients. The first part of Eq. (3) is the smallest model and the latter two parts are the smoothest model, which make the model smooth in both the horizontal and the vertical directions. The final objection function can be expressed as

$$\min : \phi = \phi_d + \alpha\phi_m, \qquad (4)$$

where ϕ_d is the data misfit function as displayed in Eq. (2), and α is the regularization parameter. Eq. (4) can be solved by an optimization algorithm such as the gradient descent method (Wang et al., 2015b).

The results of the density inversion are shown in Fig. 6. Variations in density typically indicate variations in rock type. Faults are interpreted at the boundaries between positive and negative densities.

4 Gravity data interpretation

As shown by the flow chart in Fig. 4, further interpretation of the gravity data was based on previous data processing. Meanwhile, the MT inversion result conducted by our group has also been adopted for integrated analysis. The goal of interpretation focuses on two aspects. First, this study wants to verify the existence of faults and describe their deeper extensions. Second, this study looks to identify new faults in the research area. In the following section, the discussion will focus on these aspects. Blue arrows were used to mark the major faults, pink arrows for smaller faults, and green arrows and black arrows for newly identified faults.

4.1 Analysis of existing faults

The results of the gravity inversion along the survey line were utilized to verify the existence of several faults. All of the major faults, F1–F4, have obvious characteristics in both of the two inversion results, confirming their existence. Some of the smaller faults (SF2 and SF5) have characteristics in only one of the inversions, indicating further investigation is needed to prove their existence. Table 2 shows the reliability assessment of these existing faults based on the analysis of the inversion results.

The F1 fault, named the Sauron–Ulanhot fault, is a deep fracture which extends to more than 40 km depth. It is steeply inclined at shallow depths then gradually flattens. The gravity data from this study indicate the F1 fault is cut by several other faults between 20 km and 35 km depth, but this has yet to be confirmed. Where the fault crosses the gravity survey line, the dip of F1 is to the southeast, which indicates the fault F1 may be a result of the Siberian plate's subduction to the southeast. The geological interpretation of the Sauron-Ulanhot fault is that it is an ancient subduction zone caused by the Paleo-Asian Ocean's subduction to the south under the North China craton in the Caledonian period.

The F2 fault named the Gaojia kiln–White City fault is also a deep fracture. It has an obvious signature in both the gravity and MT inversion results. It extends to depths of more than 40 km and is cut off by another fault at about 20 km. It is also cut off by SF8 at shallower depths. This has been confirmed by previous geological surveys. Compared with F1, it has a similar strike direction and better continuity in the subsurface.

The F3 fault is called the Wuyuan–Chifeng fault. Its intersection with the gravity survey line is just above the extension of the Gaojia kiln–White City fault (F2). Like the F1 fault, the F3 fault is steep near the surface but gradually flattens with depth. At a depth of about 40 km, it converges with the F4 fault to form a deep fault with longer extension.

The F4 fault is the Linhe–Harqin Banner fault. It is nearly vertical from the surface to 20 km depth, then flattens between 20 km and 30 km. At the depth about 40 km, it intersects the F3 fault.

In summary, the F1–F4 faults all extend to a deep depth. All are clearly delineated on the two inversion results. They have similar dips to the southeast which may have been caused by the continental rift and collision that took place between the Siberia plate and the North China Craton.

For the smaller faults marked as SF, not all of them have obvious signatures in the two inversion results. SF6 and SF7 were assessed to be likely faults. They extend to the depth of about 20 km. At deeper depths, no physical difference can be found in any of the inversion results. SF5 shows a possible presence on the gravity inversion result but not on the MT inversion result. Therefore, it was marked with a relatively low probability. However, nothing was found for SF2 in either of the two inversion results. So, SF2's existence should be considered carefully.

4.2 Additional potential faults

The method that the present study used to identify new faults is as follows. First, inversion results of gravity data and MT data were analyzed comprehensively to mark out the position where the fault has the highest possibility to exist along the gravity survey line. Then, these points were projected to the TDR result of the gridded gravity data in the near surface region. Finally, an integrated analysis was performed with a combination of these marks and the linear features in the TDR result to give the locations of potential faults.

In Fig. 6, the inversion results of gravity data and MT

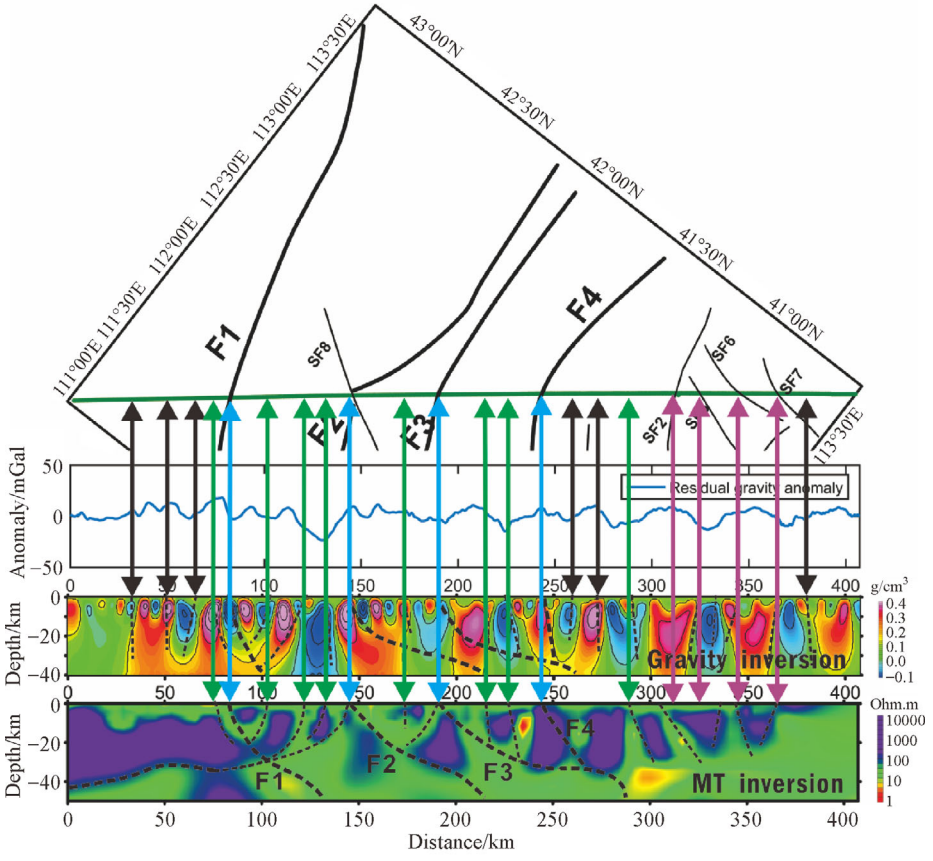

Fig. 6 Integrated analysis of the inversion results of gravity data and MT data.

Table 2 Reliability assessment of these existing faults

Number	Reliability	Description
F1	High	Obvious characteristics in both of the inversion results
F2	High	Obvious characteristics in both of the inversion results
F3	High	Obvious characteristics in both of the inversion results
F4	High	Obvious characteristics in both of the inversion results
SF1	/	Not applicable along the observation line
SF2	Lower	No obvious characteristics in the two-inversion result
SF3	/	Not applicable along the observation line
SF4	/	Not applicable along the observation line
SF5	Relatively low	Obvious characteristics in the gravity inversion result
SF6	High	Obvious characteristics in both of the inversion results
SF7	High	Obvious characteristics in both of the inversion results
SF8	High	Obvious characteristics in both of the inversion results

data were analyzed separately. Intervals between various physical parameters, which were considered as the contact between different rock blocks, were marked with black dashed lines. These two interpretation results were then studied together. Black arrows were used to mark the places which have characteristics only in one of the inversion results. These places have relatively low likelihoods of being faults. Green arrows were used to mark the places which have characteristics in both of the inversion results. These places have a relatively high possibility to be faults. The above results were projected to the TDR result of the gridded gravity data in the near

region. Potential faults would be identified by both green arrows and the linear features in the TDR result. Based on the above integrated analysis, eight new faults were identified in the near region of the gravity survey line which were named as DF1–DF8 in Fig. 7.

DF1 is parallel with the major fault F1 west of the gravity survey line and then cuts F1 to the east of the line. DF2 mirrors DF1 and cuts F1 in the same position as DF1. This phenomenon can also be seen in the two inversion results. The depth at which DF1 and DF2 intersect with F1 is about 20 km. DF3 and DF4 are nearly parallel with each other and their fault traces are almost due north. Along the gravity survey line, DF3 intersects F1 at a depth of about 35 km. On the horizontal plane, DF3 and DF4 cut F2 west of the survey line. DF5 is nearly vertical to the surface and only extends to the depth about 10 km in the subsurface. It cuts F2 east of the survey line. The trace of DF5 is nearly parallel with the major fault F1. DF6 is another fault which cuts major faults F2 and F3. Its intersection with the gravity survey line cuts F3 at the depth about 25 km. DF7 is located between faults F3 and F4. On the horizontal plane, it has an 'S' shape. Its intersection with the gravity survey line cuts F3 at the depth about 30 km which is parallel with DF6. DF8 is similar to SF1 and SF2. The inversion results show that its intersection with the survey line cuts the crust to a depth of about 20 km. An integrated use of the inversion results and the enhanced linear features of the gridded gravity data has potentially identified eight other faults in the near region of the Mongolia–Hinggan metallogenic belt. These results provide significant reference for further geological study.

5 Conclusions and discussion

Fault distribution near the Mongolia–Hinggan metallogenic belt in the eastern China-Mongolia frontier area has been studied with gravity data. The utilized gravity datasets include actual measured gravity data along a profile and gridded gravity data extracted from the WGM2012 earth's gravity model.

Based on data processing and interpretation of the gravity data, the existing faults in this area have been studied in greater detail. This study assessed their basic trace and described their deeper extensions. Meanwhile, eight new faults were also potentially identified. These results provide additional information for the in-depth understanding of the tectonic units in the eastern China-Mongolia frontier area, which also helps further understanding of the metallogenic regularities and potential prospecting directions. However, only limited geophysical research has been conducted in this area. To further understand the geological features of this area, more investigation is needed.

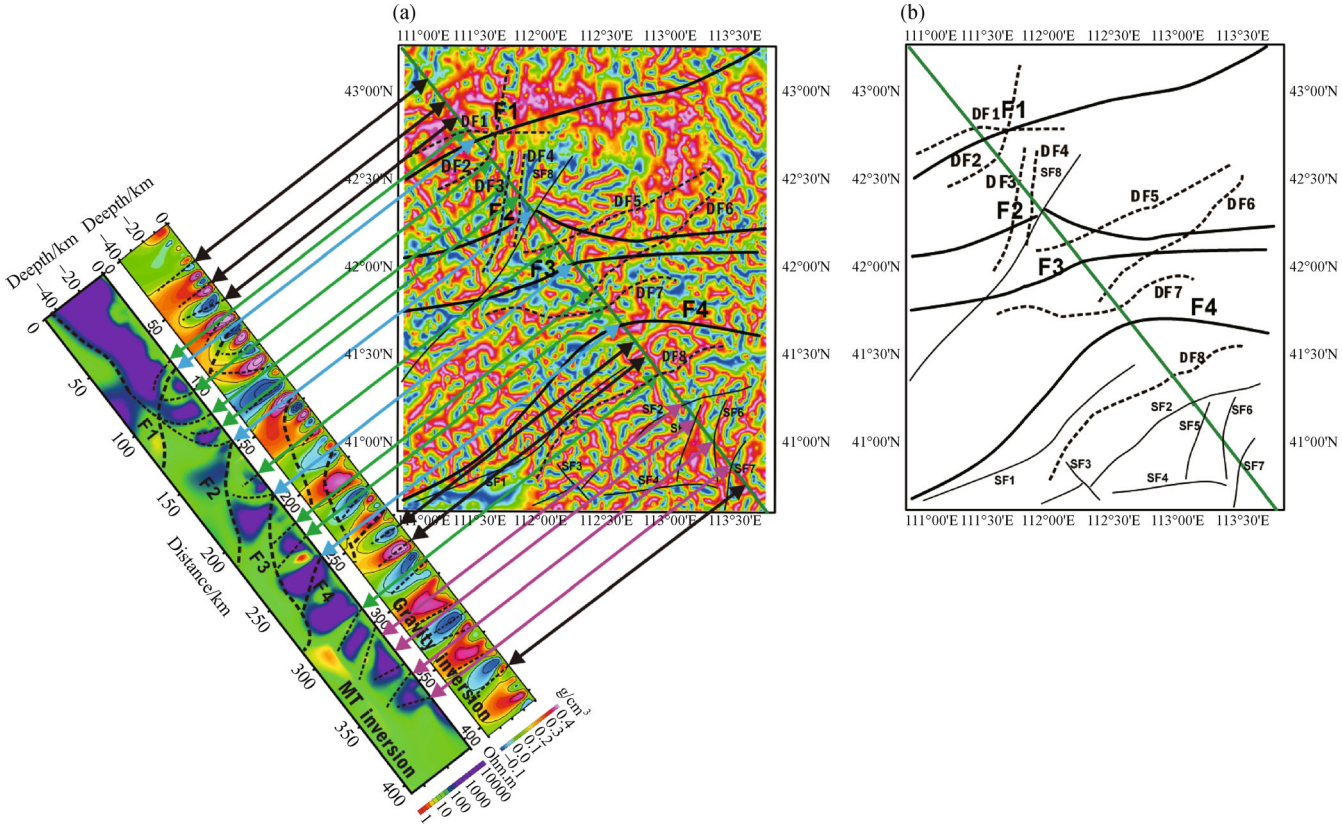

Fig. 7 Analysis of the TDR result for new potential faults in the study area.

Acknowledgements The authors thank editors and two anonymous reviewers for their suggestions in improving our paper. This work was supported by 1) The National Natural Science Foundation of China (Grant Nos. 41474106 and 41530321); 2) The National Basic Research Program of China (No. 2014AA06A613); 3) The Open Fund (NO. GDL1608) of Key Laboratory of Geo-detection (China University of Geosciences, Beijing), Ministry of Education.

References

Ali-Rahim M A (2016). Separating the gravity field of Iraq by using bidimensional empirical mode decomposition technique. Arab J Geosci, 9(1): 1–9

Amante C, Eakins B W (2009). ETOPO1 1 Arc-Minute Global Relief Model: Procedures, Data Sources and Analysis. NOAA Technical Memorandum NESDIS NGDC-24

Balmino G, Vales N, Bonvalot S, Briais A (2012). Spherical harmonic modeling to ultra-high degree of Bouguer and isostatic anomalies. J Geod, 86(7): 499–520

Blakely R J, Simpson R W (1986). Approximating edges of source bodies from magnetic or gravity anomalies. Geophysics, 51(7): 1494–1498

Chen Y, Ma J (2014). Random noise attenuation by *f-x* empirical mode decomposition predictive filtering. Geophysics, 79(3): V81–V91

Didenko A N, Kaplun V B, Malyshev Y F, Shevchenko B F (2010). Lithospheric structure and Mesozoic geodynamics of the Eastern Central Asian orogeny. Russ Geol Geophys, 51(5): 492–506

Fedi M, Florio G (2001). Detection of potential fields source boundaries by enhanced horizontal derivative method. Geophys Prospect, 49(1): 40–58

Ghosh G K (2016). Interpretation of gravity data using 3D euler deconvolution, tilt angle, horizontal tilt angle and source edge approximation of the North-West Himalaya. Acta geophysics, 64(4): 1112–1138

Guo L H, Meng X H, Zhang G L (2014). Three-dimensional correlation imaging for total amplitude magnetic anomaly and normalized source strength in the presence of strong remnant magnetization. J Appl Geophys, 111: 121–128

Huang N E, Shen Z, Long S R, Wu M C, Shih H H, Zheng Q, Yen N C, Tung C C, Liu H H (1998). The empirical mode decomposition and the Hilbert spectrum for nonlinear and non-stationary time series analysis. Proc R Soc Lond A, 454(1971): 903–995

Jahn B, Capdevila R, Liu D, Vernov A, Badarch G (2004). Sources of Phanerozoic granitoids in the transect Bayanhongor-Ulan Baator, Mongolia: geochemical and Nd isotopic evidence, and implications of Phanerozoic crustal growth. J Asian Earth Sci, 23(5): 629–653

Li L, Ji H B (2009). Signal feature extraction based on an improved EMD method. Measurement, 42(5): 796–803

Li Y G, Oldenburg D W (1998). 3-D inversion of gravity data. Geophysics, 63(1): 109–119

Liu Y, Lü Q T, Li X B, Qi G, Zhao J H, Yan J Y, Deng Z (2015). 3D gravity inversion based on Bayesian method with model order reduction. Chin J Geophys, 58(12): 4727–4739

Metcalfe I (2006). Paleozoic and Mesozoic tectonic evolution and paleogeography of East Asian crustal fragments: the Korean Peninsula in context. Gondwana Res, 9(1−2): 24–46

Miller H G, Singh V (1994). Potential field tilt – A new concept for location of potential field sources. J Appl Geophys, 32(2): 213–217

Mossakovsky A A, Ruzhentsev S V, Samygin S G, Kheraskova T N (1993). The Central Asian fold belt: geodynamic evolution and formation history. Geotectonics, 26: 455–473

Nabighian M N, Ander M E, Grauch V J S, Hansen R O, Lafehr T R, Li Y, Pearson W C, Peirce J W, Phillips J D, Ruder M E (2005). Historical development of the gravity method in exploration. Geophysics 70(6): 63ND–89ND

Nie F J, Jiang S H, Zhang Y, Liu Y, Hu P (2004). Geological features and origin of porphyry copper deposits in China-Mongolia border region and its neighboring areas. Mineral deposits, 23(2): 176–189

Nunes J C, Guyot S, Deléchelle E (2005). Texture analysis based on local analysis of the bidimensional empirical mode decomposition. Mach Vis Appl, 16(3): 177–188

Oruç B (2011). Edge detection and depth estimation using a tilt angle map from gravity gradient data of the Kozaklı-Central Anatolia Region, Turkey. Pure Appl Geophys, 168(10): 1769–1780

Perello J, Cox D, Garamjav D, Sanjdorj S, Diakov S, Schissel D, Munkhbat T O, Oyun G (2001). Oyu Tolgoi, Mongolia: Siluro-Devonian Porphyry Cu-Au-(Mo) and High-Sulfidation Cu Mineralization with a Cretaceous chalcocite blanket. Econ Geol, 96(6): 1407–1428

Phillips J D, Hansen R O, Blakely R J (2007). The use of curvature in potential-field interpretation. Explor Geophys, 38(2): 111–119

Uieda L, Barbosa V C F (2012). Robust 3D gravity gradient inversion by planting anomalous densities. Geophysics, 77(4): G55–G66

Verduzco B, Fairhead J D, Green C M, MacKenzie C (2004). New insights into magnetic derivatives for structural mapping. Leading Edge (Tulsa Okla), 23(2): 116–119

Wang J, Meng X H, Guo L H, Chen Z X, Li F (2014). A correlation-based approach for determining the threshold value of singular value decomposition filtering for potential field data denoising. Journal of Geophys and Engineering, 11 (5): 055007

Wang J, Meng X H, Li F (2015a). Improved curvature gravity gradient tensor with principal component analysis and its application in edge detection of gravity data. J Appl Geophys, 118: 106–114

Wang J, Meng X H, Li F (2015b). A computationally efficient scheme for the inversion of large scale potential field data: application to synthetic and real data. Comput Geosci, 85: 102–111

Williams S E, Fairhead J D, Flanagan G (2005). Comparison of grid Euler deconvolution with and without 2D constraints using a realistic 3D magnetic basement model. Geophysics, 70(3): L13–L21

Xiao W J, Huang B C, Han C M, Sun S, Li J L (2010). A review of the western part of the Altaids: a key to understanding the architecture of accretionary orogens. Gondwana Res, 18(2−3): 253–273

Yan J Y, Lu Q T, Wu M A, Chen X B, Zhang K, Qi G (2014). Prospecting indicator of Anhui Shaxi porphyry copper deposits based on regional gravity and magnetic 3D inversion. Acta Geol Sin, 88(4): 507–518

Yarmolyuk V V, Kuzmin M I, Ernst R E (2014). Intraplate geodynamics and magmatism in the evolution of the Central Asian Orogenic Belt. J Asian Earth Sci, 93: 158–179